Ocean Engineering 36 (2009) 974–984

Contents lists available at ScienceDirect

Ocean Engineering

journal homepage: www.elsevier.com/locate/oceaneng

Downwind sail aerodynamics: A CFD investigation with high grid resolution

Ignazio Maria Viola *

Yacht Research Unit, University of Auckland, Private Bag 92019, Auckland, New Zealand

ARTICLE INFO

Article history:
Received 8 November 2008
Accepted 22 May 2009
Available online 6 June 2009

Keywords:
Sailing yacht
Downwind sail
CFD
Wind tunnel
Benchmark
High grid resolution
Direct simulation
RANS
Spinnaker
Mainsail

ABSTRACT

A computational fluid dynamics (CFD) code was applied to an America's Cup Class Yacht to investigate sailing performance in a downwind configuration. Apparent wind angles at 45°, 105° and 120° are reported, sailed with mainsail and asymmetrical spinnakers. Numerical results are in good agreement with wind tunnel data. A large mesh investigation was performed, ranging from 60,000 elements up to 37 million elements, which shows a converging trend to the experimental values with differences smaller than 3% in both lift and drag. The most commonly used turbulence models in sail applications were tested and the results are presented here in two meshes with 1 million elements and 6.5 millions, respectively. All turbulence models over-estimate forces more than solving the Navier–Stokes system without any additional equations, hence turbulence models do not increase solution accuracy according to these results.

1. Introduction

The present work was carried out as part of a wider Ph.D. research project with the aim of setting up a computational fluid dynamic (CFD) tool to investigate the aerodynamics of an America's Cup (AC) Yacht. Since the nineties, the exponential increase of the available computational resources motivated all the America's Cup challengers to investigate the ability of a Navier–Stokes solver to compute marine fluid dynamics problems and to replace inviscid codes that were largely used since the sixties. In the last two AC editions, Politecnico di Milano wind tunnel has conducted wind tunnel tests for *Prada Challenger* in the 31st AC and for *Lunarossa Challenger* in the 32nd AC, respectively. In 2004, Lunarossa has financed the Ph.D. grant with the aim of taking advantage of the large amount of experimental data available from wind tunnel tests. Several sailplans were numerically investigated and good agreement between experimentally measured and numerically computed global forces was achieved. Therefore, CFD has become a useful design tool, in particular to investigate the flow field with the visualization capabilities of the numerical computation and generally to improve the understanding of sail aerodynamics. In the present work, the main achievements about downwind sails are summarized and three configurations are described, at 45°, 105° and 120° apparent wind angles (AWA), respectively, to include most of the downwind sailed conditions in the last AC.

At closer apparent wind angles, that is in upwind conditions, the flow is mainly attached therefore non-viscous codes can well predict aerodynamic forces. On the other hand, at larger angles, the flow is mainly separated on sail perimeters; hence global forces are less responsive to computational parameters. In the AWA range investigated, both separated and attached flow regions have a strong influence on force production, where lift is about twice the drag force. The flow around the spinnaker presents a turbulent cavitation nucleus along the luff (i.e. leading edge), where a secondary laminar cavitation nucleus (difficult to be detected) plays an important role in the first nucleus size (Collie and Gerritsen, 2006). Normally, the discretization adopted does not allow either of the two cavitation nuclei. The reattached flow presents an accelerated boundary layer velocity profile that is hard to resolve with a standard computational wall function. Finally, there is a leach (i.e. trailing edge) separation strongly connected to the tip vortex generated at the foot (i.e. root) and at the head (i.e. tip) of the sail. The flow around the mainsail might be fully attached or separated. The studied phenomena present most of the current challenges for computational fluid dynamics: transition, re-attachment, re-laminarization, both laminar and turbulent separations. Pressure measurements on sails and flow field visualization will allow future comparison of CFD local results with experimental data, but at the present time only global forces are available.

* Tel.: +64 9 5275046, +64 21 682925(Mobile).
E-mail address: im.viola@auckland.ac.nz

0029-8018/$ - see front matter © 2009 Elsevier Ltd. All rights reserved.
doi:10.1016/j.oceaneng.2009.05.011

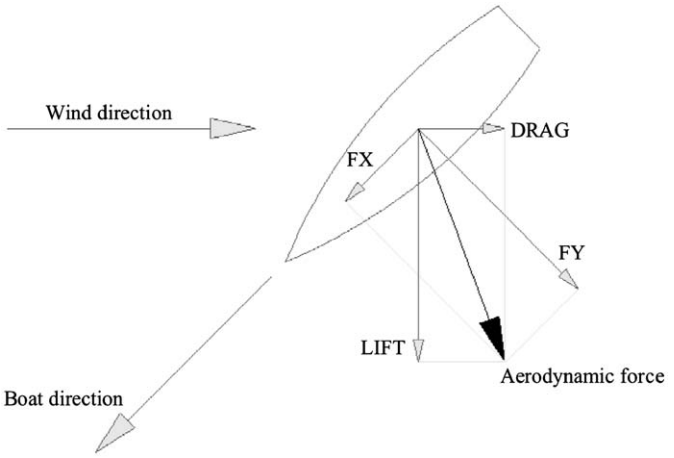

Fig. 1. Terminology, wind direction (hence drag and lift axis) is defined at the reference height of 10 m full-scale.

In the following, the terminology presented in Fig. 1 will be adopted. The X and Y axes are, respectively, thrust and side directions with respect to the longitudinal axes of the yacht model. The aerodynamic force includes forces acting on every part of the yacht above the water plane, hence windage effects are not subtracted. The horizontal components are generally resolved as thrust and side components, or alternatively drag and lift, where drag is aligned with the reference wind direction and lift is perpendicular to the wind. The vertical component, i.e. along Z-axis, will not be discussed in the present work. Incoming flow has a vertical velocity gradient and a vertical twist (Fossati et al., 2006), hence a reference height at 10 m full-scale was adopted to define a reference wind speed and wind direction. Apparent wind angle is defined as the angle between the drag axis and the X-axis. Force components are expressed in terms of non-dimensional coefficients defined as follows:

$$C_D = \frac{drag}{0.5\rho V^2 S}; C_L = \frac{lift}{0.5\rho V^2 S};$$
$$C_X = \frac{thrust\_force}{0.5\rho V^2 S}; C_Y = \frac{side\_force}{0.5\rho V^2 S} \quad (1)$$

where ρ is density, V and S are, respectively, reference wind speed and sail area.

Leeway angle is ignored as it is common practice in wind tunnel tests to correct the AWA to take into account the leeway angle when running a velocity prediction program (VPP).

2. State of the art

In the following, a state of the art overview is presented with the aim of putting in evidence the increase capabilities of the CFD techniques in sailing yacht applications, mainly due to the exponential growth of the computational resources.

The first numerical simulations of sails were conducted in the sixties with inviscid codes at the Massachusetts Institute of Technology, where Milgram developed vortex lattice methods and flat wakes to investigate upwind sails. This work were published in 1968 (Milgram, 1968a, b). A few years later, in 1971, Gentry working for the aerospace *Boeing Company* of Seattle was investigating the mainsail and jib interaction with a panel method plus boundary layer solutions (Gentry, 1971). This work was reviewed and updated 10 years later by Gentry himself (1981), and most of his applications in the America's Cup design were described in Gentry (1988).

In the nineties, the increasing computational resources available made numerical codes the primary design tool in advanced sail design. The well-known *North Sails* designer Burns Fallow described the computer-aided design process of the successful Team New Zealand challenge to the 1995 AC (Fallow, 1996). The challenge to the AC by the New Zealand Yacht Squadron gave a strong impulse to the aerodynamics of sailing yacht research at the University of Auckland. In 1993, Hedges reported in her M.E. thesis (Hedges, 1993) the first downwind RANS application: she adopted a finite-volume RANS solver named *CFDS-FLOW3D* with a $k-\varepsilon$ turbulence model as described in Hedges et al. (1996). A structured mesh of hexahedral elements was used. Because of the reduced computational capabilities in 1993, the spinnaker was resolved by less then 400 elements against the average of over 200,000 elements in the present work. Hedges compared computed global coefficients with wind tunnel forces measured at 90° AWA. She tested several boom and pole angles to maximize the thrust force achieving a maximum lift (aligned with thrust axis at 90° AWA) which was 15% lower than the experimental data, and with a 3% difference between numerical and experimental drag. The comparison did not include the hull and at 90° AWA the flow field was mainly attached. A small mesh and standard turbulence model could work adequately, because the investigated flow field had a small amount of separated flow.

The second RANS application was performed by Miyata and Lee at the Tokyo University in 1999 on an upwind configuration with an in-house-code and Baldwin–Lomax turbulence model (Miyata and Lee, 1999). The mesh was still a structured hexahedral and it was non-conformal along a surface between the main and jib to save grid points and did not stretch the cells in between. They created a conformal mesh to compare results and no significant differences were reported. Computed thrust force coefficient C_X was over-estimated by less than 28% and side force coefficient C_Y was under-estimated by less than 18% compared to wind tunnel data for every tested AWA between 15° and 35°.

More recently, Collie performed a large investigation upon turbulence models for sail applications, mainly based on two-dimensional (2D) simulations. In Collie et al. (2001), the authors wrote a review of the turbulence models to be used in sail flow analysis, reporting comments and a detailed ranking for: $k-\varepsilon$ (simply named ke in the following), $k-\varepsilon$ with low-Re correction, $k-\omega$ in the original formulation, $k-\omega$ modified by Wilcox in 1998 (kw in the following), $k-\omega$ shear-stress transport (sst), $k-\tau$, Spallart–Almaras (sa) and algebric-stress-model. The authors concluded that Spallart–Almaras model performed better in the upwind conditions and the $k-\omega$ shear-stress transport model in downwind conditions. In Collie et al. (2002a), the authors performed 2D unsteady computations (URANS) with the CFD code Fluent testing the implemented models $k-\varepsilon$: the original formulation (ke), the formulation described by the re-normalization group (rng) theory and the more recent formulation named realizable (rlz). Benchmarks were primarily performed on the backward facing step problem with a structured hexahedral mesh and $y+$ about 20 in the near-wall region. The more recent rlz model performed better then the older turbulence models and, hence, the authors supposed that it was adequate to simulate upwind conditions. A similar turbulence model test was performed with the code *CFX* and the implemented models ke, kw and sst, testing a horizontal spinnaker section (Collie et al., 2002b). The mesh was similar: structured hexahedral and $y+$ about 1 in the near-wall region. The sst model followed the experimental coefficient trends better with AWA and, hence, the authors supposed it was adequate to simulate downwind conditions. In both the Fluent and *CFX* tests, the 2D formulations did not accurately model 3D flow, thus numerical/experimental absolute global-force differences were quite significant. In Collie

and Gerritsen (2006), the authors carried out another 2D computation to compare with experiments on a flat plate at low angles of incidence performed by Crompton and Barrett (2000). With a similar mesh and $y+$ smaller than 1, kw and sst models were compared and the sst model confirmed to perform better than the kw model. In this case, the numerical/experimental comparison showed very good agreement between both global forces and local measurements.

The first downwind RANS computation with tetrahedra was published by Richter et al. (2003). To have a smaller mesh size in the near-wall region they performed a local refinement. This work presented an innovative aero-elastic coupling between the CFD code *Fluent* (*Ansys Inc*) and the FE code *MemBrain* (*North Sails Inc.*) and no experimental comparison was presented.

In the last two years, several authors have published numerical/experimental comparisons on upwind configurations: Yoo and Kim (2006), and Yoo et al. (2006), with a structured mesh of 1.7 million (M) cells and $y+<50$, obtained differences between numerical and experimental values less than 83% in lift and 59% in drag; Ciortan and Soares (2007), with 1 M of tetrahedral elements and prismatic layers to reach $135<y+<270$, showed differences lower than 86% in lift and 50% in drag; Querard and Wilson (2007), with 2.4 M of hexahedral cells and $y+$ of the order of (O(.) in the following) 10, obtained differences lower than 12% in lift and 24% in drag; Masuyama et al. (2007), with a structured mesh of 0.5 M hexahedra and $y+=\mathrm{O}(1)$ published qualitative differences in agreement with Viola (2008), who adopted 1.5 M of tetrahedral elements and prismatic layers to reach $y+=\mathrm{O}(1)$ achieving differences less than 3% in lift with a systematic overestimation and less than 6% in drag.

On downwind configurations, RANS analyses were reported by Lasher and Richards (2007), and by Lasher and Sonnenmeier (2008). In the second work, the authors tested 12 spinnakers and six turbulence models (ke, rlz, rng, kw, sst, rsm), with 0.33 and 0.14 M of tetrahedra and $30<y+<120$, obtaining averaged differences with wind tunnel data between 11% and 7% in lift, and between 12% and 5% in drag. The authors focused on turbulence model differences and tested only two (similar) meshes that returned relative differences of about 5%.

In the present work, three different downwind AWA's are simulated and compared, each with a 6 M element mesh. The numerical/experimental ratios of the coefficients are less than 8% for both lift and drag. A large investigation on the dependence of the solution on mesh size and topology is also presented. In particular, meshes up to 37 M elements (larger by more than 100 times any mesh found in the references, for downwind condition) were tested. These exhibit a converging trend towards the experimental values (differences less than 3% in lift and 2% in drag). Furthermore, the turbulence models, sa, ke, rlz, and sst, were tested on two meshes, 1 M elements with $y+=\mathrm{O}(30)$ and 6.5 M elements with $y+=\mathrm{O}(10)$, respectively. All turbulence models over-predict the forces and increase the problem complexity without appreciable improvement in solution accuracy.

3. Wind tunnel tests

Wind tunnel test were performed at the Politecnico di Milano twisted flow wind tunnel in the boundary layer test section. More details about the test section and the flow quality are published in Fossati et al. (2006). Special devices to twist the incoming flow and model the changes in the apparent wind speed with height were adopted. More details about the twisted vanes device can be found in Zasso et al. (2005).

Fig. 2. Lunarossa model scale in the boundary layer test section of the Politecnico di Milano twisted flow wind tunnel sailing at 45° AWA.

The model scale was 1:12.5 to have a large model without an excessive blockage effect. Model height was $h=2.7$ m. Because the wind tunnel test section is 4 m height and 14 m wide, and a typical AC class sailing area is 800 m^2, the blockage of the model was approximately 0.1.

Model yacht drum-type sheets were operated through a seven channel proportional radio control system, except that the antenna was replaced by a hard wire link and the usual joystick transmitter was replaced by a console with seven multi-turn control knobs that allowed winch drum positions to be recorded and re-established if necessary. The sail trimmer, who operated from the wind tunnel control room, controlled the sheet trims. A six-component balance was placed inside the yacht hull. The data acquisition software calculated the forces and moments using the dynamometer calibration matrix. The forces were shown in the virtual panel designed on the computer screen in real time so that the sail trim could be optimized, because the effects of trimming the sails on the driving and heeling forces could be directly appreciated.

Fig. 2 shows a standard test at 45° AWA. Behind the model, the twisted vanes device and also the wide extension of the test section (about 40 m long) which allows the boundary layer to be generated are visible. More details about the test procedure are published in Fossati et al. (2006).

Immediately after the force measurements, an operator went inside the wind tunnel and took pictures with a high-resolution camera. Images were collected together and a three-dimensional mathematical flying shape was reconstructed with a dedicated software.

Three sailplan configurations are reported at three AWA's: 45°, 105° and 120°. Nominal apparent wind angle is defined as the angle between the boat longitudinal axis and the undisturbed incoming apparent wind at 10 m height from the water plane, which coincides with wind tunnel longitudinal axes. Two asymmetric spinnakers were considered, A1 and A4, where the identification number increases with the design apparent wind angle range. Hence, A1 was sailed at 45° AWA and A4 at 105° and 120° AWA. The same mainsail A2 was sailed at every angle.

Mainsails were built with horizontal mylar panels and asymmetric spinnakers with tri-radial polyester panels, hence similar materials to full-scale but with smaller thickness.

4. Numerical setup

The Navier–Stokes equations were solved with the RANS technique. Sail aerodynamics can be considered a relatively high Reynolds number (4×10^5, computed on the model height h) and a low Mach number (7×10^{-3}) flow and, hence, density variation can be neglected and Navier–Stokes equations can be presented as

$$\nabla \cdot u^* = 0$$
$$(u^* \cdot \nabla)u^* = -\nabla p^* - \frac{1}{\mathrm{Re}}\nabla^2 u^* \quad (2)$$

where u^* and p^* are, respectively, the non-dimensional velocity and pressure, Re the Reynolds number,∇ the gradient operator and $\cdot$ the scalar product.

In Eq. (2), it can be observed that the only scale index is presented by the Reynolds number. Hence, it must be the same in numerical computation and experimental test. The full-scale Reynolds number is almost 10 times larger but it is usually unobtainable in a wind tunnel test because of fragility of the model.

The flow field around the sail is mainly turbulent and a number of grid points of the order of $\mathrm{Re}^{9/4} = 4 \times 10^{11.5}$ might be used to compute all the turbulence scales from the largest which draw energy from the mean flow to the smallest that extract energy for viscous dissipation. In the present work up to 4×10^7 cells were used, therefore, turbulence models were tested to verify if any additional enhancement could be achieved taking into account the grid-filtered small-scale effect in the averaged flow field. Additional turbulence model equations did not return significant advantages as reported in Section 7.

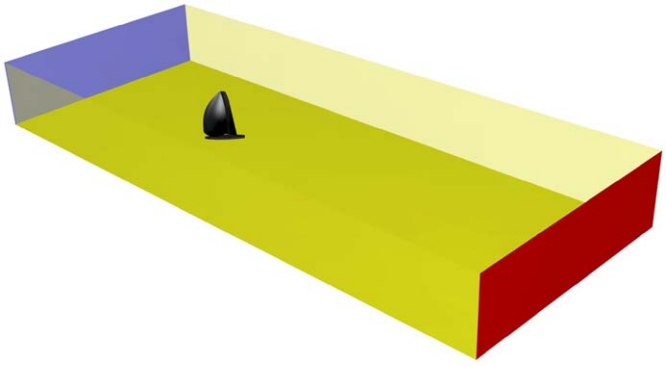

Fig. 3. The computational domain at 45° AWA: black color show the sails and the hull; the inflow surface is blue; the outflow surface is red and the slip condition is applied on the yellow surfaces.

Computed global forces are compared with measured forces in terms of non-dimensional coefficients of drag and lift components or thrust and side force component. Force components perpendicular to the horizontal plane are much less meaningful and were neglected in the present publication.

Center of effort height CEH is reported vertically from the water plane and is divided by the boat's model height h. It is computed by dividing the heeling moment by the side force.

For each of the three sail configurations, at 45°, 105° and 120° AWA, respectively, the following procedure was applied: a 3D model of the hull and the sails, which were modelled with no thickness, was used to trim a box 15h length, 6h wide and 1.3h height. In particular, the boat model is located in the box 5h from the inlet box face and 10h from the outlet box face. A smaller wind tunnel cross section was modelled to avoid modelling the wall velocity profile, hence a slip condition was imposed on the water plane, on both sides and on the top of the computational box. The model is 3h from both sides and the top of the mast is 0.3h from the top of the box (Fig. 3). The boom was taken into account by extending the lower edge of the mainsail. The mast was modelled only in the most accurate grid.

A tetrahedral mesh was adopted because of its flexibility in modelling complex 3D geometries. The commercial preprocessors *Gambit v*2.4.6 and *Tgrid v*5.0.6 (*Ansys Inc.*), which are based on a bottom-up approach, were used to build the meshes because of their efficient algorithms for triangular and tetrahedral grids, respectively. Four different mesh sizes of 0.06, 1, 6.5 and 37 M were used and observed differences are discussed in Section 6. In particular, the sail and hull surface grids were performed in *Gambit* with equisized triangles with edge lengths of 0.037h, 0.0074h, 0.0026h and 0.0011h, respectively. A growth rate lower than 1.3 was adopted building the triangular grid of the box surfaces (Fig. 4). The grid of all the surfaces was imported in *Tgrid* where the tetrahedral cells were built, also with a growth rate lower than 1.3. No prism layers were used.

*Fluent v*6.3.26 (*Ansys Inc.*) was used in the implicit pressure-based steady formulation, with a SIMPLE scheme and first-order discretization.

A preliminary test showed that first-order upwind discretization, applied to both pressure and momentum equations, led to a better convergence than the second-order upwind. However, deeper investigations on higher order accuracy are necessary.

5. Numerical results

In Fig. 5, the three sail trims are presented and the corresponding aerodynamic force is plotted. The force vector is

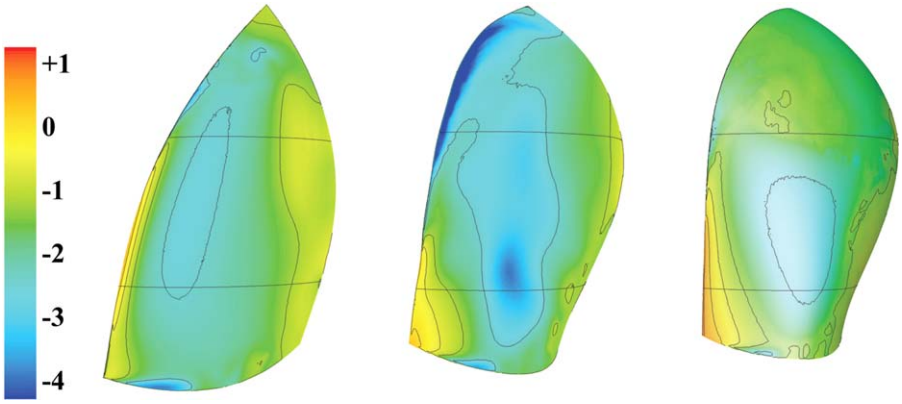

Fig. 4. The most coarse grid (0.06 M cells) at 45° AWA: triangles are equisized on the sails and on the hull, then triangle size increases on the water plane with a growth rate lower than 1.3.

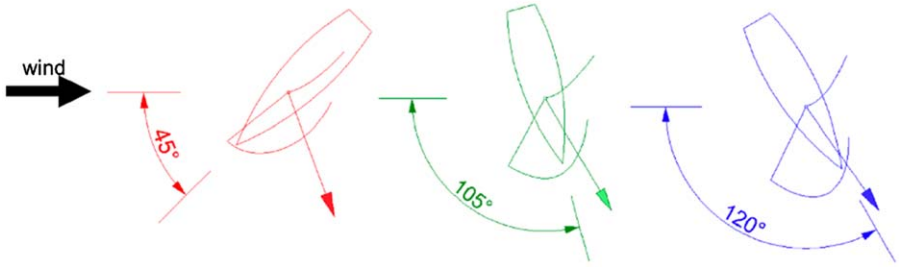

Fig. 5. Apparent wind angle, boat direction, sail position and resultant aerodynamic force vector are sketched for the three reported conditions.

Table 1
Numerical/experimental lift and drag ratios for 45°, 105° and 120° apparent wind angles, with a 6.5 M cells mesh and without turbulent model.

AWA	45°	105°	120°
$CD^{num/exp}$	1.06	1.00	1.08
$CL^{num/exp}$	0.99	1.08	1.00

scaled and oriented for the three AWA's. The sails are always in a similar position with respect to the wind direction that comes horizontally from the left in each sketch. However, when increasing AWA the boat direction changes and the asymmetric was trimmed to obtain a deeper horizontal shape. The figure shows that the order of magnitude and the direction of the aerodynamic force are similar for each AWA but that the projection on the boat course changes significantly. Despite this, the flow field changes appreciably as is shown below.

In Table 1, the numerical/experimental coefficient ratios are presented for the lift and drag components and for the three AWA's. Data are obtained with the 6.5 M cell mesh without the turbulent model. Numerical results are in good agreement with experimental data. The differences are always less than 8%.

In Fig. 6, the asymmetric spinnaker flying shapes are shown from the lift axis (leeward perspective) and pressure coefficient distributions are plotted for 45°, 105° and 120° AWA, respectively. Red regions indicate high pressure and blue regions indicate lower pressure as shown by the color bar on the left. Black lines show iso-pressure values: $Cp = 0.5,\ 0,\ -0.5,\ -1,\ -2$ and the two horizontal lines indicate the $\frac{1}{3}h$ and $\frac{2}{3}h$ reference heights for the following figures. The pressure coefficient is defined as follows:

$$Cp = \frac{p - p_0}{0.5\rho V^2} \tag{3}$$

where p is the local static pressure, p_0 the reference pressure on the outflow boundary, ρ the density and V the reference wind speed. The figure shows the flying shapes exposed to the wind, and the vertical position of the minimum pressure region changing with the increasing AWA.

Figs. 7–9 show non-dimensional dynamic pressure coefficient q^* distribution at $\frac{2}{3}h$ and $\frac{1}{3}h$ reference heights for 45°, 105° and 120° AWA, respectively. Red regions show high-speed areas and blue regions are low-speed areas as shown by the color bar. Lines are iso-pressure values: $Cp = 0.5, 0, -0.5, -1$ and -2. The dynamic pressure coefficient q^* is defined as follows:

$$q* = \frac{u^2}{V^2} \tag{4}$$

where u is the local velocity and V the reference velocity.

The figures show that the flying shape horizontal sections change with increasing AWA: sections become deeper and the differences between the upper and lower sections increase. The low-speed region (dark blue) on the leeward side of the sails indicates separated flow. The flow is separated in the higher sections at 45° AWA and attached in the lower sections. At 105° AWA, the reverse occurs, the lower sections are deeper than the higher ones. At 120° AWA, the flow is still attached only in a small region on the leeward side of the asymmetric and the flow on the leeward side of the mainsail is fully separated.

Figures from 10 to 15 show Cp curves onto $\frac{1}{3}h$ (left) and $\frac{2}{3}h$ (right) reference heights, respectively, for 45°, 105° and 120° AWA. Curves are plotted versus non-dimensional chord length. The blue and the red curves show asymmetric spinnaker and mainsail Cp's, respectively. In Fig. 10, the blue curve shows a typical pressure distribution for a high cambered profile: pressure decreases on the leeward side of the asymmetric up to about 30% of the chord line, then both pressure and its adverse gradient increase until separation occurs and pressure becomes constant. On the windward side, pressure coefficient increases up to 1.0 where local static over-pressure ($p-p_0$) is equal to the inflow dynamic pressure ($0.5\rho V^2$). When the flow is fully separated, the pressure profile is almost constant along the chord. (Figs. 10–15).

6. Mesh sensitivity investigation

In the present work, an AMD Opteron 275 dual core processor with 74 nodes at 2.2 GHz each with 2 GB RAM allowed the solution of large fully tetrahedral meshes. Four similar meshes were built for the 45° AWA configuration. The computational effort and the performances can be found in Viola et al. (2008).

Fig. 16 shows computed lift and drag coefficients divided by the experimental values for the four meshes at 45° AWA. No turbulence model was used. The figure shows that in increasing the number of cells from 60,000 to 37 million, the coefficients seems to converge to the experimental values: differences between computed and experimentally measured global coefficients are more than 5% with 1 M elements and smaller than 3% with 37 M elements. Fig. 17 shows a trend of $y+$ decreasing as the number of cells increased on the asymmetric horizontal section at $\frac{1}{3}h$ with $y+$ computed as follows:

$$y^+ = y \cdot \frac{1}{\nu}\sqrt{\frac{\tau_w}{\rho}}; \tag{5}$$

where y is first cell-centre-height from the wall, ν viscosity, ρ density and τ_w wall shear stress.

Meshes have similar growth rate which are less than 1.3 (the ratio between the linear dimension of two adjacent cells in the wall normal direction) and a similar maximum element sizes. Hence, decreasing the element size in the near-wall region

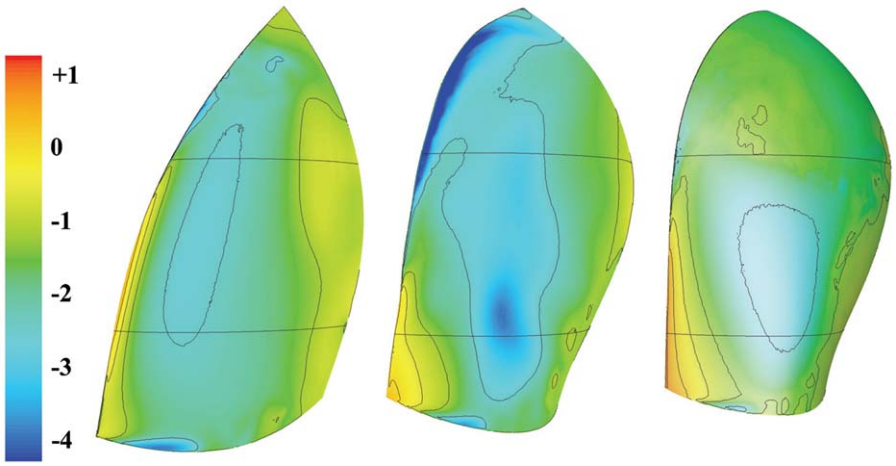

Fig. 6. Contours of pressure coefficient on leeward side of the asymmetrics at 45°, 105° and 120° AWA, respectively; iso-pressure values are tracked for $Cp = 0.5, 0, -0.5, -1, -2$.

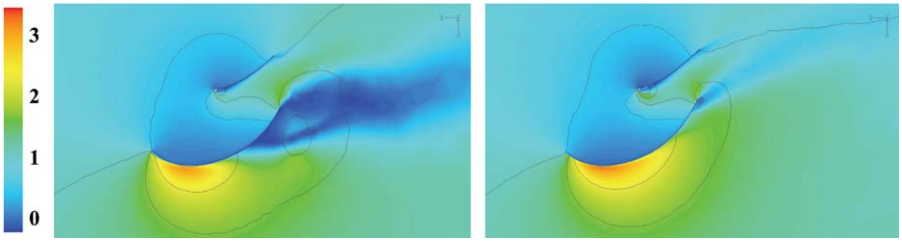

Fig. 7. Non-dimensional dynamic pressure contours at 45° AWA for $\frac{2}{3}h$ and $\frac{1}{3}h$, respectively, iso-pressure values are tracked for $Cp = 0.5, 0, -0.5, -1, -2$.

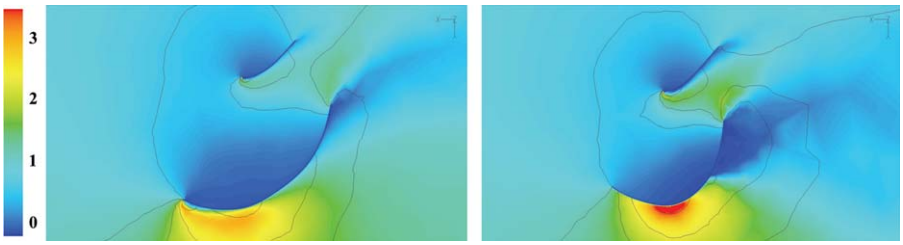

Fig. 8. Non-dimensional dynamic pressure contours at 105° AWA for $\frac{2}{3}h$ and $\frac{1}{3}h$ respectively, iso-pressure values are tracked for $Cp = 0.5, 0, -0.5, -1, -2$.

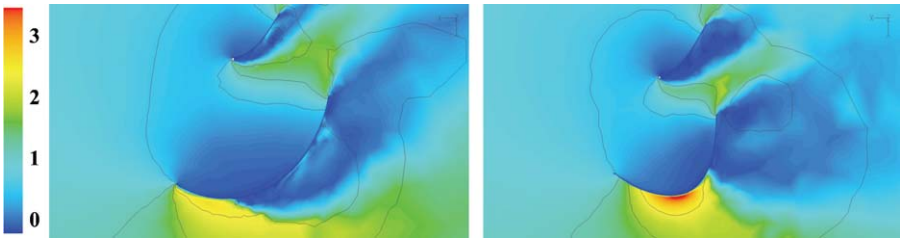

Fig. 9. Non-dimensional dynamic pressure contours at 120° AWA for $\frac{2}{3}h$ and $\frac{1}{3}h$, respectively, iso-pressure values are tracked for $Cp = 0.5, 0, -0.5, -1, -2$.

decreases both the first cell-centre-height and $y+$, while there is an increase in overall number of elements and also the degree of freedom to be solved and the corresponding computational effort increases. This approach allows several topologically identical meshes to be built, but with an increasing space resolution. It is a computationally expensive approach but it permits investigating the effect of the space resolution when it is not know a priori where the lack of resolution mostly affects the computed solution. In fact, tetrahedral elements, with a growth rate less than 1.3, without refinements and non-conformal faces, minimize the mesh influence on the solution but, on the other hand, lead to an expensive growth of the number of elements to solve the near-wall region gradients. In particular, $y+ = O(30)$ with meshes of the order of 1 M cells, were adopted in the most recent works (Lasher and Richards, 2007; Lasher and Sonnenmeier, 2008). In the present work, 37 M elements were used to reach $y+ = O(5)$. To obtain smaller $y+$ values without increasing the number of elements, many authors have adopted hexahedral or prismatic

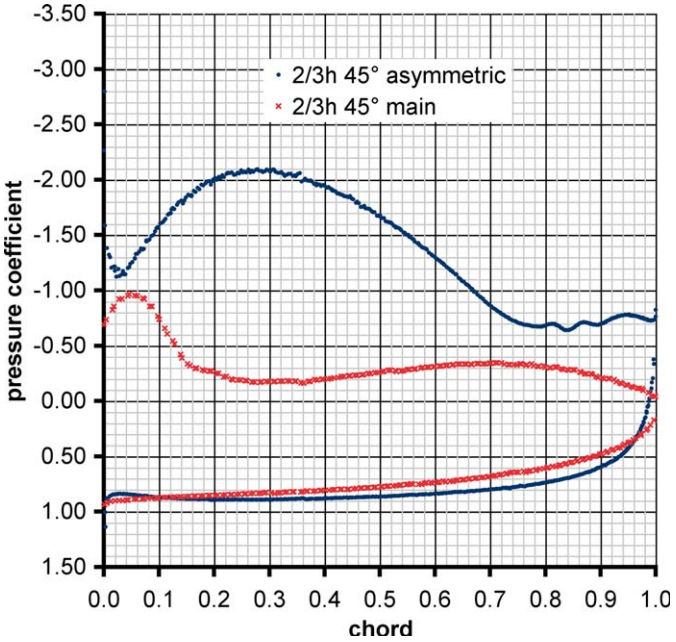

Fig. 10. Pressure coefficients along sail chords of mainsail and asymmetric at 45° AWA and $\frac{2}{3}h$.

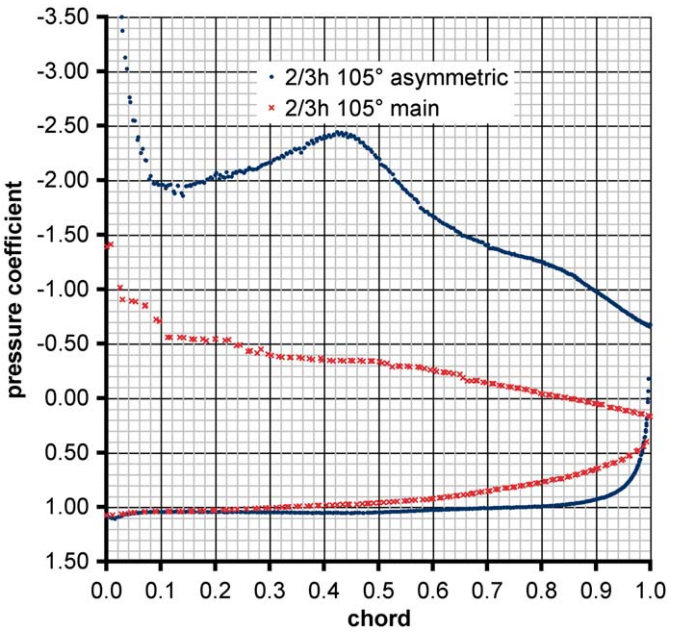

Fig. 12. Pressure coefficients along sail chords of mainsail and asymmetric at 105° AWA and $\frac{2}{3}h$.

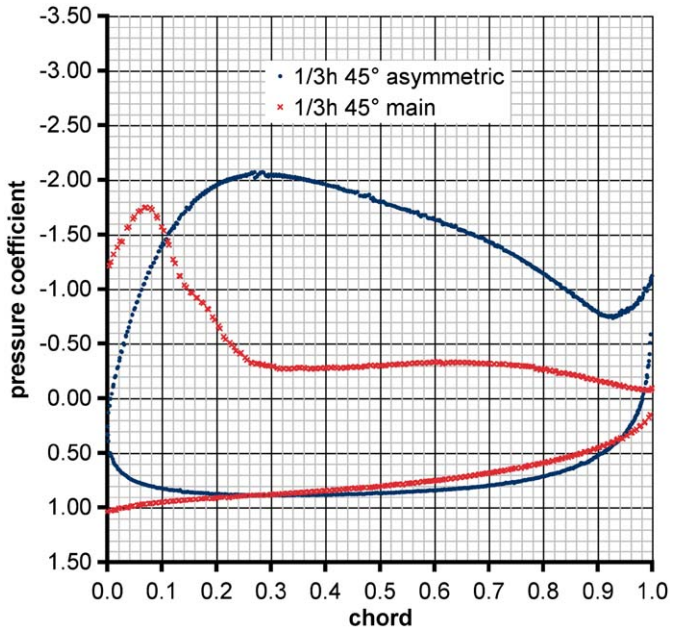

Fig. 11. Pressure coefficients along sail chords of mainsail and asymmetric at 45° AWA and $\frac{1}{3}h$.

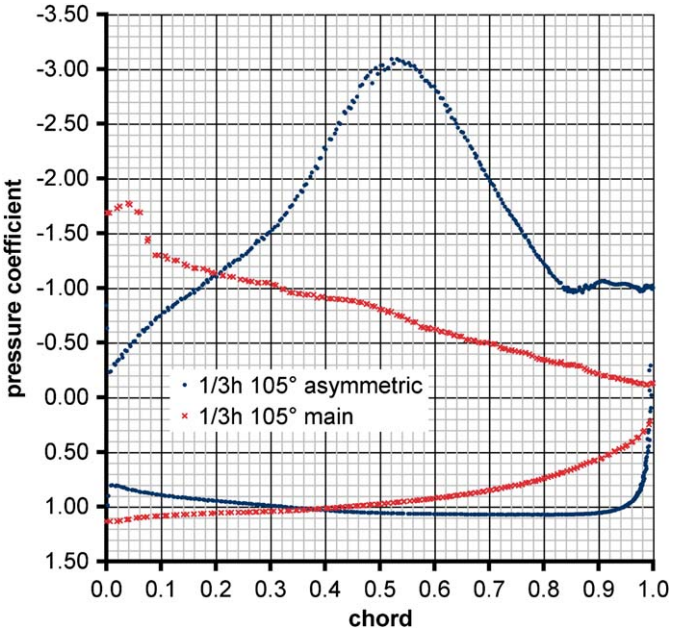

Fig. 13. Pressure coefficients along sail chords of mainsail and asymmetric at 105° AWA and $\frac{1}{3}h$.

elements. In fact, hexahedra and prism elements generate structured grids which can be compressed along one dimension. Hence, they allow grid refinement along one direction without increasing excessively the overall number of elements. On the other hand, stretched hexahedra or prisms produce an anisotropic behavior of the discrete derivative operator. Hence, they might induce an anisotropic derivative field. It is well known that linear system solver techniques perform more efficiently onto an equally spaced grid in all directions (Stueben, 2001). As an example, Fig. 18 shows non-dimensional vorticity contours on a horizontal section at $\frac{1}{3}$ of the height of a model yacht sailing in an upwind condition, computed with tetrahedral elements and with prismatic elements, respectively. The vorticity is the curl of the velocity and, hence, it involves the discrete derivate operator. The two sail sections, the jib and the main, present on the leeward side a high vorticity region shown in red. In particular, on the left, where tetrahedral elements allow isotropic grid spacing, the high vorticity region is only in the sail boundary layers and wakes. On the right, where stretched prismatic cells are adopted in the boundary layers and along four lines starting from the sail edges and ending on the domain borders, the vorticity distribution is affected by the grid anisotropic spacing and, in particular, a high vorticity region in the mainsail wake is significantly extended in the cell stretching direction (top right in figure). More details

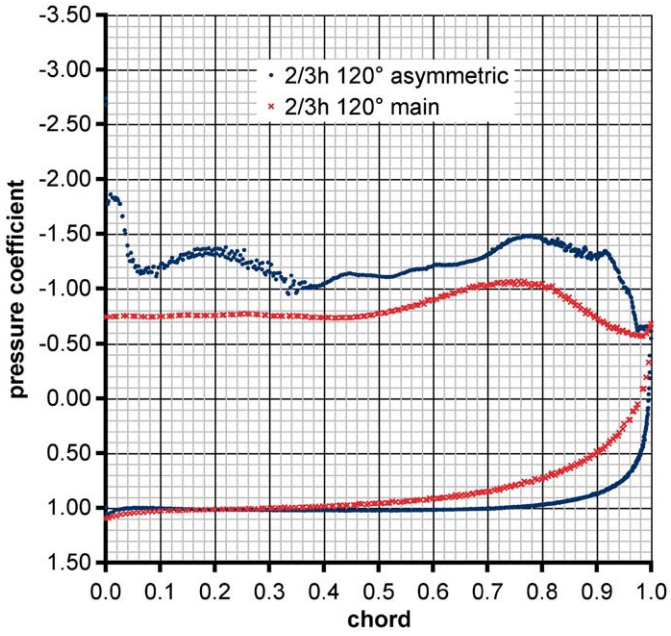

Fig. 14. Pressure coefficients along sail chords of mainsail and asymmetric at 120° AWA and $\frac{2}{3}h$.

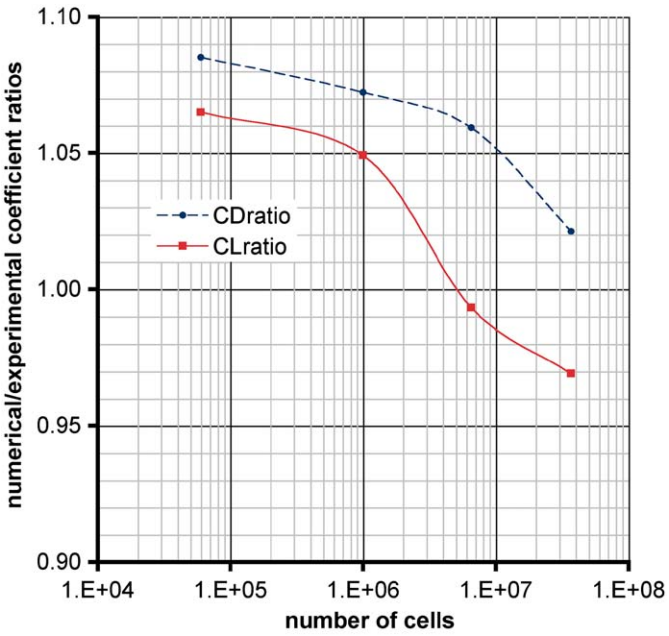

Fig. 16. Numerical/experimental coefficient ratios versus grid resolution.

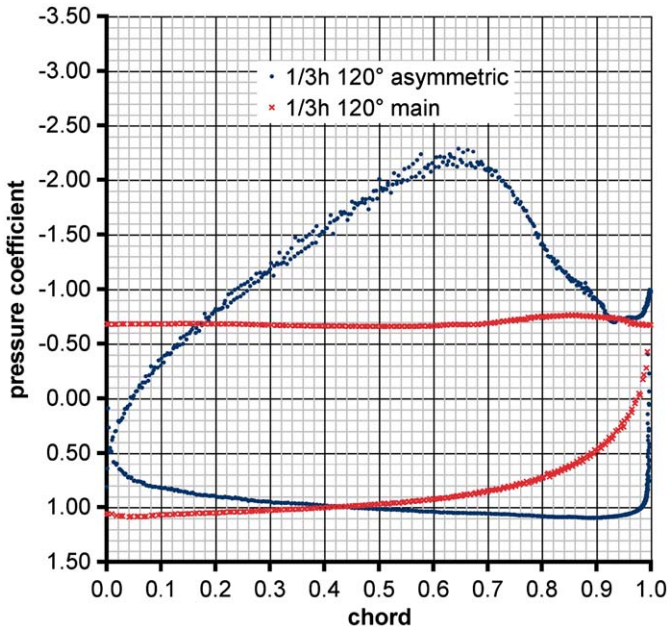

Fig. 15. Pressure coefficients along sail chords of mainsail and asymmetric at 120° AWA and $\frac{1}{3}h$.

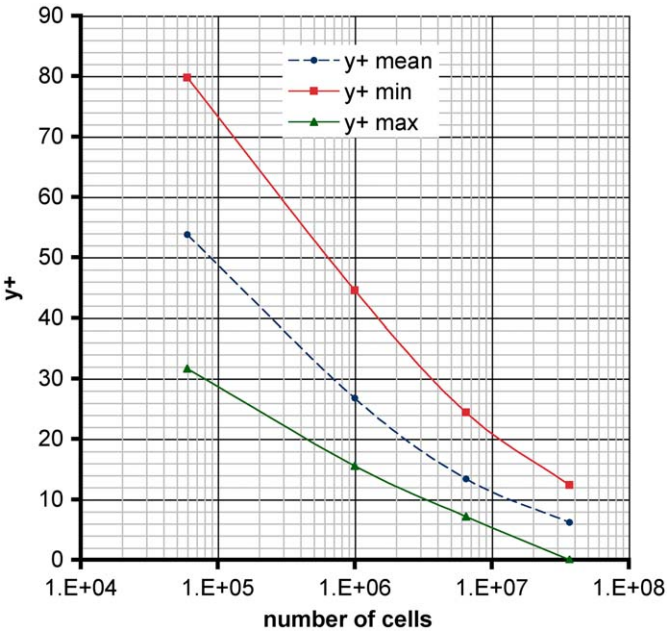

Fig. 17. Non-dimensional first cell-centre height versus grid resolution.

about the simulation reported in Fig. 18 can be found in Viola (2008).

Another aspect that might be considered is the transition from the prism region to the tetrahedral region when both element types are adopted, as performed in Ciortan and Soares (2007). For example, the same upwind geometry presented in Fig. 18 was meshed with tetrahedral elements except for the near-wall region, where 10 prismatic layers were adopted. In Figs. 19 and 20, two different meshes were used with the same growth rate, but the first prism layer height in Fig. 19 is half of that shown in Fig. 20. The two mesh schemes are shown in the figures. The transition from the prismatic region to the tetrahedral region in the case with the lowest prismatic height is more abrupt than in the case with the highest prismatic height. As a consequence, the two regions do not correctly communicate with each other and separation occurs inside the prismatic region but does not propagate into the tetrahedral region. Fig. 19 shows the velocity vector field with the low prismatic region: the thin sail presence generates a velocity profile that separates on the leeward side but separation occurs only in the prismatic region and it does not affect the tetrahedral region. In Fig. 20, the same location along the sail is focused on but meshed with a higher prismatic region: the velocity profile inverts both in the prismatic region and in the tetrahedral region.

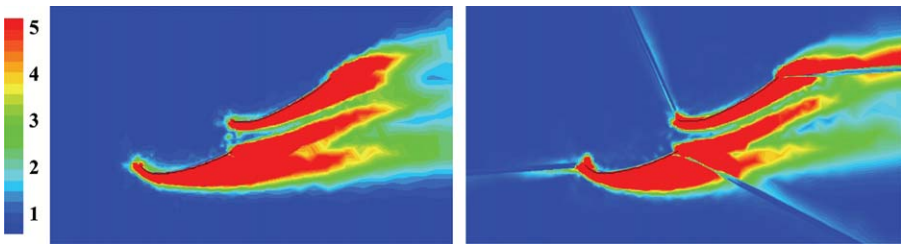

Fig. 18. Vorticity contours on an horizontal section in upwind condition computed with tetrahedral elements (left) and prismatic elements (right), showing the anisotropic behavior of the derivative operator.

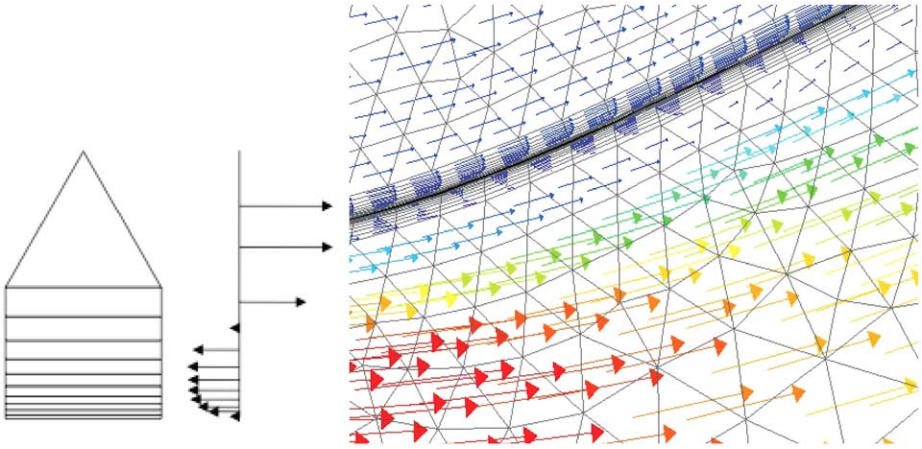

Fig. 19. Low prismatic region, separation occurs only inside the prismatic region.

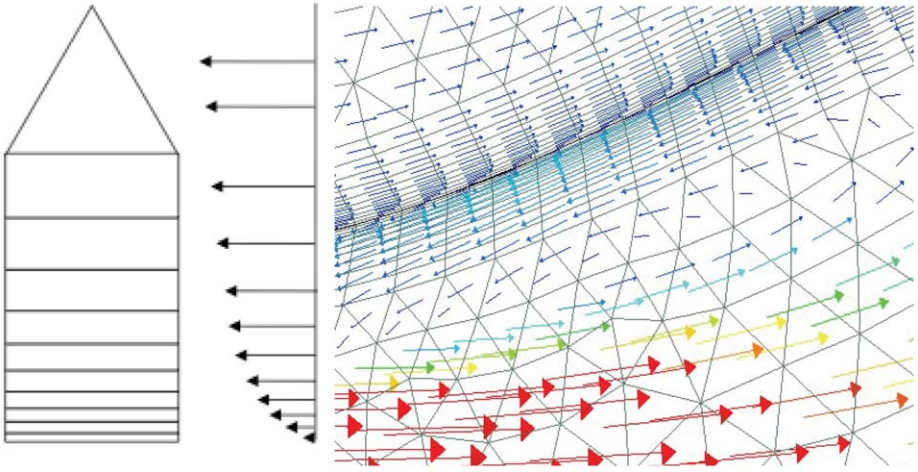

Fig. 20. High prismatic region, separation occurs inside and outside the prismatic region.

7. Turbulence models

To perform a Direct Navier–Stokes computation, the number of cells used should be of the order of one tera-elements but at the present day it is still unaffordable. Therefore, turbulence models can be used to take into account the grid-filtered fluctuation effects on the averaged flow field. Models require one (e.g. sa) or two (e.g. ke and kw) additional equations to be solved and most of the formulations are not able to relax turbulent quantities when the flow speed is significantly reduced in the near-wall region (namely, low-Reynolds correction). Hence, wall functions have to be implemented adding new equations to be solved. On the other hand, turbulence models are far from being universal models applicable to any flow condition and wall functions are well known to work incorrectly with separated flow, so several corrections could be implemented to let them model separated boundary layers. Therefore, turbulence models should be applied only if a significant accuracy increase is achieved. The following results show that against the increasing complexity and arbitrariness of the equation system to be solved, turbulence models do not increase significantly accuracy. On the other hand, turbulence models increase significantly the stability of the solution and show a fast convergence.

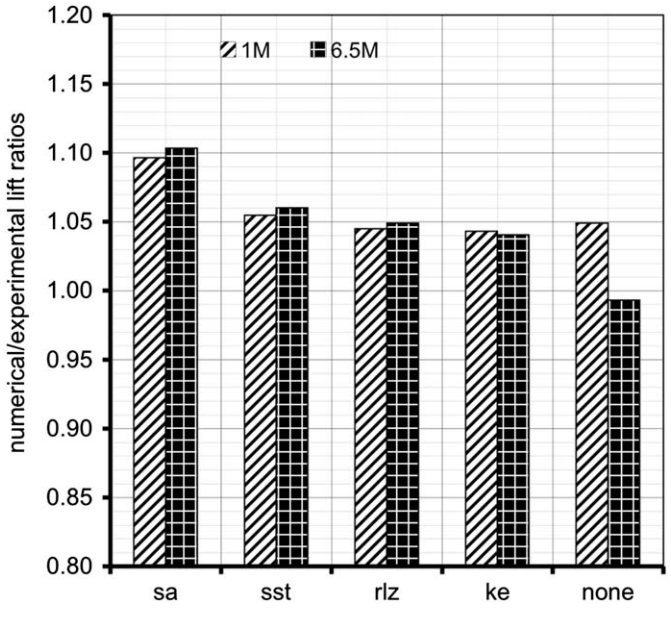

Fig. 21. Numerical/experimental lift ratios computed with several turbulence models.

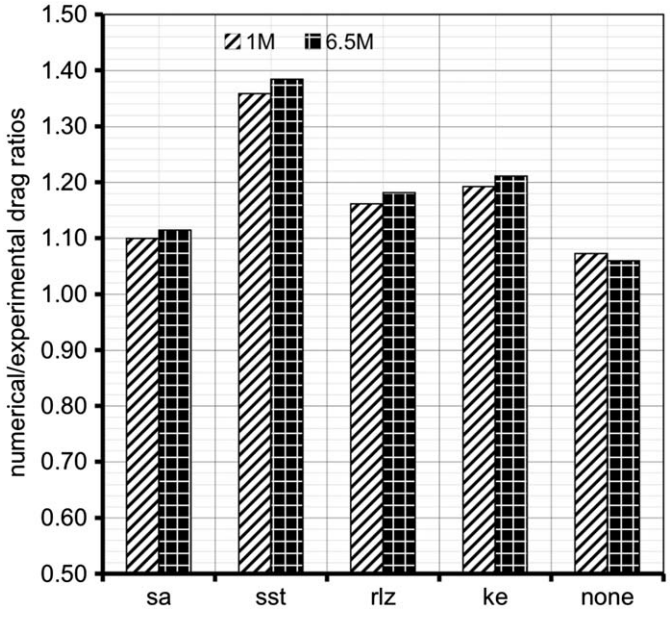

Fig. 22. Numerical/experimental drag ratios computed with several turbulence models.

At the current state of the art of downwind sail applications, turbulence models were tested with large $y+$ and hence with wall functions. Therefore, in the present work the Fluent implemented *non-equilibrium* wall function was adopted. Six turbulence models were tested with two meshes: 1 M elements with $y+ = O(30)$ and 6.5 M elements with $y+ = O(15)$, respectively. The first cell-centre of the coarser mesh should be in the so-called logarithmic layer and the cell-centre of the finer mesh should be in the buffer layer between the viscous sub-layer and the logarithmic layer.

The following models were tested: sa, sst, klz, ke. Two thousands iterations were performed for each of them starting from the solution obtained without any turbulence model. Each of them converged to a new force value. Figs. 21 and 22 show lift and drag numerical/experimental coefficient ratios, respectively, obtained without any models (named none in figure) and with the four models. The models are presented in order of predicted lift ratio values computed with the 6.5 M cell mesh. All of them over-predict lift components more than the computation without any turbulence model and this result does not depend on mesh size. All models over-predict lift independently of mesh size, but there is no correlation between drag and lift over-prediction order.

8. Conclusions

A CFD code was used to investigate the aerodynamics of downwind sails. An America's Cup Yacht (version 5), with an M2 mainsail and A1 asymmetric spinnaker sailing at 45° AWA and A4 sailing at 105° and 120°, respectively, was studied. The flow field was investigated with 6.5 million of tetrahedral cells without any turbulence model. In the 45° AWA configuration, a grid study was performed with 0.06, 1, 6.5 and 37 M of tetrahedral cells and four turbulence models were tested with 1 and 6.5 M cell grids.

Numerically computed aerodynamic forces were compared with wind tunnel forces measured in the Politecnico di Milano twisted flow wind tunnel.

The numerical analysis of the flow field leads to the following conclusions:

- The flow is mainly attached on the two sails when sailing at 45° AWA; trailing edge separation occurs on the highest part of the asymmetric spinnaker, where the sail is deepest.
- The reverse occurs at 105° AWA, because the sail is deeper in the lowest part: trailing edge separation occurs on the lowest part of the asymmetric spinnaker.
- At 120° AWA, the flow is mainly separated on the leeward side of the two sails.
- The maximum *Cp* on the two sails is about 1 at the leading edge on the windward side, showing a correct computation of the stagnation point.
- The minimum *Cp* is about −3 on the asymmetrical spinnaker and higher than −2 on the mainsail.
- Increasing the AWA causes the maximum chamber of an horizontal section of the asymmetrical spinnaker to move backward. As a consequence, the minimum *Cp* also moves backward along the chord. On the horizontal section at $\frac{1}{3}h$, the minimum *Cp* is at about 30%, 50% and 65% of the chord length at 45°, 105° and 120° AWA, respectively.

The flow fields investigated depend on the sail shapes and trims, hence different results might be found by other authors studying the same three AWA conditions.

The computed forces are in good agreement with the wind tunnel forces, differences are lower than 8% for every AWA. The following remarks can be made:

- Increasing the number of grid cells, a converging trend of the computed forces to the experimental values was achieved, with differences smaller than 3% in lift and 2% in drag.
- No asymptotic trend was observed and a grid-independent solution was not achieved, regardless of the high number of cells adopted. Hence, further investigation on high accuracy grids are necessary.
- The first discretization order was adopted to achieve more stable solutions but higher discretization orders might be tested in a further study.

The four more common turbulence models, sa, sst, rlz, ke, were tested with two meshes with 1 and 6.5 M cells, respectively.

In particular:

- All the turbulence models show a systematic over-estimation of the forces.
- The force over-estimation do not depend on the grid size, regardless to the position of the first cell-centre. The 1 M cells grid have $y+ = O(30)$ and the first cell-centre is in the so-called logarithmic layer; the 6.5 M cells grid have $y+ = O(15)$ and the first cell-centre is in the buffer layer between the viscous sub-layer and the logarithmic layer.
- The model which shows the maximum over-estimation of one force component is different from the model which shows the maximum over-estimation of the other coponent. In particular:
  - The sa model shows the maximum lift over-estimation and the more accurate drag.
  - The sst model shows the maximum drag over-estimation.
  - The sst, rlz and ke models show a similar lift over-estimation.
- The simulations performed with turbulent models are less sensible to the grid size compared to the simulations performed without the turbulent models. The grid dependency of the computations performed without turbulent model shows that the grid is filtering flow fluctuations which have a significant effect on the mean flow. In fact, increasing the accuracy of the grid, which is the equivalent of changing the filter, leads to a significant force reduction. On the other hand, each turbulent model takes into account the grid-filtered fluctuations in a different way, leading to large differences in the force prediction.

In conclusion, it seems that the increased computational complexity associated with the turbulence models tested did not lead to more accurate results in this work.

Acknowledgements

Authors would like to thanks sail designers Guido Cavalazzi, Henrik Soderlund, Grant Spanhake and yacht designer coordinator Claudio Maletto of Lunarossa 32nd AC Challenger who have always supported and believed in this research; Giuseppe Passoni and Raffaele Ponzini for their precious suggestions.

References

Collie, S., Gerritsen, M., 2006. The Challenging Turbulent Flows Past Downwind Yacht Sails and Practical Application of CFD to Them. In: proceedings of the Second High Performance Yacht Design Conference, Auckland, New Zealand.

Collie, S.J., Gerritsen, M., Jackson, P., 2001. A Review of Turbulence Modelling for Use in Sail Flow Analysis. School of Engineering Report no. 603, Auckland, New Zealand.

Collie, S., Gerritsen, M., O'Sullivan, M., 2002a. Numerical Simulation of the Turbulent Flow Past Upwind Yacht Sail. Submitted to Journal of Wind Engineering and Industrial Aerodynamics.

Collie, S., Jackson, P., Gerritsen, M., 2002b. Validation of CFD Methods for Downwind Sail Design. In proceedings of the High Performance Yacht Design Conference, Auckland, New Zealand.

Ciortan, C., Soares, C.G., 2007. Computational study of sail performance in upwind Condition. Ocean Engineering 34, 2198–2206.

Crompton, M., Barrett, R., 2000. Investigation of the separation bubble formed behind the sharp leading edge of a flat plate at incidence. In proceedings of the Institution of Mechanical Engineers, Part G 214, 157–176.

Fallow, J.B., 1996. America's cup sail design. Journal of Wind Engineering and Industrial Aerodynamics 63, 183–192.

Fossati, F., Muggisca, S., Viola, I.M., Zasso, A., 2006. Wind Tunnel Techniques for Investigation and Optimization of Sailing Yachts Aerodynamics. In: proceedings of the Second High Performance Yacht Design Conference, Auckland, New Zealand.

Gentry, A.E., 1971. The Aerodynamics of Sail Interaction. In: proceedings of the Third AIAA Symposium on the Aero/Hydronautics of Sailing, Redondo Beach, California, USA.

Gentry, A.E., 1981. A Review of Modern Sail Theory. In: proceedings of the 11th AIAA Symposium on Sailing, Seattle, Washington, USA.

Gentry, A.E., 1988. The Application of Computational Fluid Dynamics to Sails. In: proceedings of the Symposium on Hydrodynamic Performance Enhancement for Marine Applications, Newport, Rhode Island, USA.

Hedges, K.L., 1993. Computer Modelling of Downwind Sails. ME Thesis, University of Auckland, New Zealand.

Hedges, K.L., Richards, P.J., Mallison, G.D., 1996. Computer modelling of downwind sails. Journal of Wind Engineering and Industrial Aerodynamics 63, 95–110.

Lasher, W.C., Richards, P.J., 2007. Validation of RANS simulations for international America's cup class spinnaker force coefficients in an atmospheric boundary layer. Journal of Ship Research 51 (1), 22–38.

Lasher, W., Sonnenmeier, J., 2008. An analysis of practical RANS simulations for spinnaker aerodynamics. Journal of Wind Engineering and Industrial Aerodynamics 96, 143–165.

Masuyama, Y., Tahara, Y., Fukasawa, T., Maeda, N., 2007. Database of Sail Shapes vs. Sail Performance and Validation of Numerical Calculation for Upwind Condition. In: proceedings of the 18th Chesapeake Sailing Yacht Symposium, Annapolis, Maryland, USA.

Miyata, H., Lee, Y.W., 1999. Application of CFD simulation to the design of sails. Journal of Marine Science and Technology 4, 163–172.

Milgram, J.H., 1968a. The aeodynamic of sails, In: proceedings of the Seventh Symposium of Naval Hydrodynamic, pp. 1397–1434.

Milgram, J.H., 1968b. The analytical design of yacht sails. In SNAME Annual Meeting 13, 118–160.

Querard, A.B.G., Wilson, P.A., 2007. Aerodynamic of Modern Square Head Sails: a Comparative Study Between Wind-Tunnel Experiments and RANS Simulations. In: proceedings of the Modern Yacht, Southampton, UK.

Richter, H.J., Horrigan, K.C., Braun, J.B., 2003. Computational Fluid Dynamics for Downwind Sails. In: proceedings of the 16th Chesapeake Sailing Yacht Symposium, Annapolis, USA.

Stueben, K., 2001. Introduction to Algebraic Multigrid. In: Oosterlee, C.W., Trottenberg, U., Schuller, A. (Eds.), Academic Press, New York, USA.

Viola, I.M., 2008. Fluidodinamica Numerica e Sperimentale Applicata alla Dinamica delle Imbarcazioni a Vela (Numerical and Experimental Flow Dynamics applied to Sailing Yacht Dynamics). Ph.D. Thesis, Politecnico di Milano, Milan, Italy.

Viola, I.M., Ponzini, R., Rocchi, D., Fossati, F., 2008. Analysis of Aerodynamic Indices for Racing Sailing Yachts: a Computational Study and Benchmark on up to 128 CPUs. In: Proceeding of the 20th International Conference on Parallel Computational Fluid Dynamics (PARCFD2008), Lyon, France.

Yoo, J., Kim, H.T., 2006. Computational and experimental study on performance of sail of a sailing yacht. Ocean Engineering 33, 1322–1342.

Yoo, J., Kim, J., Park, I., Ahn, H., Van, S., 2006. CFD Calculation on the Sail Like Three Dimensional Airfoils. In: proceedings of the Second High Performance Yacht Design Conference, Auckland, New Zealand.

Zasso, A., Fossati, F., Viola, I.M., 2005. Twisted Flow Wind Tunnel Design for Testing Yacht Sails. In: proceedings of EACWE4 European and African Conference on Wind Engineering, Praga, Ceca Republic.